Energy 360 2 (2024) 100012

Contents lists available at ScienceDirect

Energy 360

journal homepage: www2.cloud.editorialmanager.com/engy/default2.aspx

Optimizing biomass briquette drying: A computational fluid dynamics approach with a case study in Mozambique

Fauzia Argentina Guibunda [a,b,*], Sebastian Waita [a], Francis Wanjala Nyongesa [a], G. Jeffrey Snyder [b], Jimmy Chaciga [c]

[a] Department of Physics, University of Nairobi, P.O. Box 30197–00100, Nairobi, Kenya
[b] Department of Material Science and Engineering, Northwestern University, Evanston, IL 60208, USA
[c] Department of Physics, Makerere University, P.O. Box 7062, Kampala, Uganda

ARTICLE INFO

Keywords:
Charcoal briquette
Computational Fluid Dynamics (CFD)
Open sun drying
Solar tunnel dryer

ABSTRACT

Biomass fuels remain the primary cooking energy source in many developing regions, contributing to deforestation and greenhouse gas emissions. Briquettes made from waste biomass are a sustainable alternative; however, their production is hindered by inefficient drying methods, such as open sun drying, which can take 5 to 7 days. This study evaluates the thermal and airflow performance of a solar tunnel dryer (STD) designed to accelerate drying times for charcoal briquettes under Mozambique's climatic conditions. Using Computational Fluid Dynamics (CFD) simulations, temperature and airflow distributions were analyzed to optimize dryer performance. Moisture and temperature profiles of hexagonal briquettes with inner holes indicated effective drying, achieving uniform moisture reduction to 10 % from an initial 50 %. Drying time was projected based on simulated airflow and temperature conditions, showing a significant reduction compared to traditional methods. The STD, operating with air temperatures of 36.5 °C to 65 °C and velocities up to 33.5 m/s at a mass flow rate of 1.36 kg/s, demonstrated its potential to enhance briquette production efficiency while maintaining environmental sustainability. The findings underscore the viability of solar drying technology for biomass fuel processing.

1. Introduction

Globally, biomass briquette drying is critical in producing sustainable solid fuels but poses challenges due to high energy consumption and lengthy drying times. Efficient drying methods are vital for enhancing the economic viability and sustainability of biomass fuels by reducing energy requirements and improving fuel quality. Traditional drying techniques often rely on fossil fuels or inefficient processes, leading to considerable environmental impacts, such as greenhouse gas emissions and air pollution (Ndukwu et al., 2020; Lamrani et al., 2022). As the demand for renewable energy sources grows, improving biomass drying methods has gained importance to minimize the carbon footprint and lower production costs, especially in energy-limited regions.

Solar-assisted drying technologies have emerged as an environmentally and economically viable solution to address these challenges. Solar dryers, particularly solar tunnel dryers (STDs), and solar dehumidification systems represent sustainable alternatives to conventional drying methods (Tuncer et al., 2020). By harnessing solar energy, these systems can achieve substantial energy savings and reduce the drying time of biomass briquettes. Recent advances in Computational Fluid Dynamics (CFD) have enabled the design of more efficient drying systems, allowing researchers to analyze airflow and temperature distribution within dryers to optimize energy transfer and airflow (Ameri et al., 2018). In the last five years, significant progress has been made in developing solar drying systems across Africa, driven by research into region-specific designs and optimized performance under local environmental conditions. Studies have focused on improving the thermal efficiency of solar dryers by integrating features such as finned and baffled designs, which enhance heat transfer and air circulation to achieve uniform and accelerated drying (Kasaeian et al., 2018).

In Africa, solar drying research has shown substantial promise. Studies in Kenya, Ghana, and South Africa have tested various solar drying technologies and have reported promising results, such as reduced drying times and energy savings, validating solar dryers as sustainable options for rural and peri-urban communities (Dhar et al., 2020; Mewa et al., 2019). For example, solar dryers with latent heat

* Corresponding author at: Department of Physics, University of Nairobi, P.O. Box 30197–00100 Nairobi, Kenya.
E-mail address: guibunda.fauzia@gmail.com (F.A. Guibunda).

https://doi.org/10.1016/j.energ.2024.100012
Received 11 October 2024; Received in revised form 16 November 2024; Accepted 28 November 2024
Available online 30 November 2024

storage systems have been developed to sustain drying at night, increasing the versatility and efficiency of solar drying methods in sub-Saharan climates (Raj et al., 2019). These innovations have laid the groundwork for applications in other African countries with high solar potential and similar socio-economic needs for sustainable biomass processing. Mozambique, with its significant solar energy potential, offers an ideal case study to illustrate the broader applications of solar drying technologies. The current study investigates the airflow and temperature distribution within a solar tunnel dryer designed specifically for drying charcoal briquettes in Mozambique. Using CFD-based analysis, this research examines three distinct dryer configurations to identify optimal designs for drying efficiency under varying solar radiation conditions. This work contributes to the scientific understanding of renewable energy applications in biomass drying, providing insights relevant to both local policy and sustainable energy practices across sub-Saharan Africa.

2. Materials and methods

2.1. CFD modeling approach for solar tunnel dryers

The CFD methodology is designed to adapt to diverse climatic settings, facilitating application across various geographic regions. This model integrates location-specific climatic variables, including solar irradiance, ambient temperature, humidity, and wind speed, enabling flexibility in simulating different environmental conditions. Such a generalized approach accommodates regions where local weather may significantly impact drying efficiency and thermal performance. This section outlines the CFD model's fundamental principles, design considerations, and configuration parameters, highlighting adjustments based on geographic factors to ensure broad applicability. Numerical simulations are performed using Fluent software, employing the CFD method to analyze airflow and thermal dynamics inside the solar tunnel dryer system.

2.2. Case study: applying the CFD model in Mozambique

2.2.1. Case study setup for Mozambique

To demonstrate the adaptability and effectiveness of this CFD model, it is applied to a case study in Mozambique, a region characterized by climatic variability that poses unique challenges for biomass drying. Mozambique's geographic coordinates (10°27'S to 26°52'S latitude and 30°12 W to 40°51 W longitude) are used to set solar radiation parameters accurately within the model. This case study centers on a large-scale drying system designed for Verde Africa Ltd, a briquette production facility that requires an effective solution to reduce the initial moisture content of wet briquettes from approximately 50 % (wet basis) to 10 % (wet basis), a crucial process for producing high-quality, storable briquettes.

2.3. Description of the solar tunnel dryer for Mozambique

The general design framework of the solar tunnel dryer (STD) features a forced convection system optimized for large-scale drying, specifically for biomass fuels like charcoal briquettes. The dryer structure includes a drying chamber where the drying product is placed, a solar air heater (SAH) for preheating incoming air, and a moveable drying bed for uniform airflow distribution. Axial fans are employed to maintain consistent airflow and temperature levels. The drying chamber is designed with a trapezoid frame structure, which supports a UV-stabilized transparent polyethylene cover to maximize solar heat absorption. A double-opening door provides efficient loading and unloading while minimizing heat loss, and a concrete foundation enhances the system's durability. This generalized design is versatile, supporting diverse applications with adjustments based on specific environmental parameters such as solar irradiance and airflow requirements.

Table 1
Design specifications and assumptions.

Design Conditions and Assumptions		
Parameters		**Specifications**
Orientation		East – West Direction
Drying Product		Charcoal Dust Briquette
Loading Capacity		1120kg
Dryer Efficiency		45%
Temperature of Air Stream		60 °C
Temperature of Briquette		50 °C
Diameter-Dryer		4m
Moisture Content	*Initial*	50%
	Final	10%
General Conditions		
Sunshine Hours		7.31 hrs
Global Solar Radiation		5.7kwh/m^2
Density of Ambient Air		1.225kg/m^3
Density of Water		997.77kg/m^3
Specific Heating Capacity of Water		4.2$kJ/kg\ K$
Specific Heating Capacity of Charcoal Dust		1.002$kJ/kg\ K$
Specific Heating Capacity of Air		1.005$kJ/kg\ K$
Latent Heat of Vaporization of Water		2260kJ/kg
Ambient Temperature		23 °C
Heat Transfer Condition		Steady State

Table 2
Dimensions of the briquette.

No.	Dimension	Amount
1	Length (L)	0.15m
2	One Side Width (S)	0.025m
3	Width (W)	0.05m
4	Height (h)	0.04m
5	Hole Diameter (Dhl)	0.015m
6	Total Number of Briquette (nt)	3200pc

Table 3
Overview of design requirements.

Technical design dimensions	
Parameters	Technical specifications
Drying System	Solar tunnel dryer
Type	Walk-In
Shape	Trapezoidal frame structure
Drying Bed	Fixed double layer
Bed Type	Movable
Number of Bed	4
Shape of Bed	T-Shape framed structure
Orientation	East-West

The Mozambique-specific solar tunnel dryer configuration features a drying chamber with dimensions of 17.5 m in length, 4 m in width, and 2 m in height, supported structurally by a concrete foundation. Detailed dimensions of the face surface of the dryer are provided in Fig. 2 to facilitate replication. The chamber is equipped with axial fans positioned at both the front and rear to ensure consistent airflow, for optimal drying conditions. The polyethylene cover, UV-stabilized for durability, maximizes solar gain while providing insulation to sustain controlled internal temperatures. Inside the chamber, four movable drying beds accommodate large batch sizes, each designed to hold approximately 1200 kg of charcoal dust briquettes, which is equivalent to about 3200 individual pieces. Each bed measures 12 m in length, 0.77 m in width, and 1.3 m in height. For smaller loads, the system also includes individual drying beds with a capacity of 300 kg, sized at 6 m in length, 0.77 m in width, and 1.3 m in height. Each drying bed is structured with 20 tiers, supported by a fixed 10-layer framework to ensure maximum exposure of the briquettes to the heated air. Technical specifications and design parameters of the solar tunnel dryer are provided in Tables 2 and

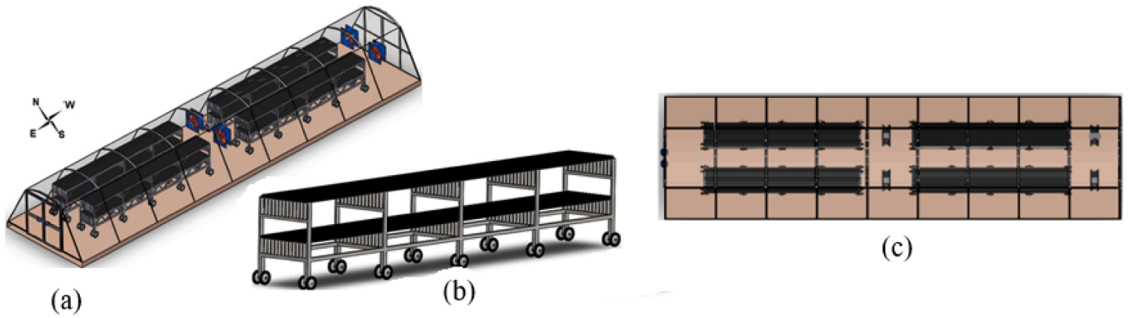

Fig. 1. Schematic diagram of the designed dryer (a), diagram of drying bed (b), and the top view of bed arrangements (c).

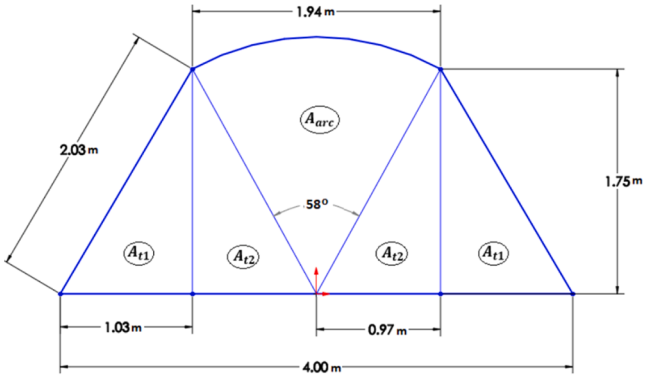

Fig. 2. Face surface dimensions of the STD.

Table 4
Drying chamber design and energy parameters.

Design Parameters	
Drying Capacity per Batch (m_{bi})	$1,120kg$
Amount of Water Removed (m_{wr})	$448kg$
Initial Moisture Wet Base (M_i)	50 %
Final Moisture Wet Base (M_f)	10 %
Final Temperature - product (T_{bf})	50 ℃
Final Temperature of Air (T_{af})	60 ℃
Ambient Temperature (T_{am})	23 ℃
Efficiency (η)	45 %
SH* Charcoal Briquette ($Q_{s,b}$)	$18.33MJ$
Sensible Heat for Water ($Q_{w,b}$)	$63.504MJ$
Latent Heat for water ($Q_{l,w}$)	$1,125.03MJ$
Total Heat Energy (Q_t)	$1,206.86MJ$
Rate of Heat Energy (Q_r)	$45.861KW$
Useful Thermal Energy (Q_u)	$362.12Whr$
Dimension and Area of Drying Chamber	
Length (L_{dc})	$17.5m$
Width (W_{dc})	$4m$
Height or Radius ($H_{dc} = R_{dc}$)	$2m$
Area (A_{dc})	$110\ m^2$
Floor Area (A_{fdc})	$70\ m^2$
Dimension and Area of Drying Bed	
Length (L_{db})	$6m$
Width (W_{db})	$0.77m$
Height (H_{db})	$1.3m$
Area (A_{db})	$12\ m^2$
Briquette Surface Area (A_{bs})	$99.5m^2$
	99.6

* Sensible Heat for Charcoal Briquette

3, with further structural details illustrated in Fig. 1(b).

2.3.1. Theoretical design of the solar tunnel design

The theoretical design of the proposed Solar Tunnel Dryer was developed based on specific conditions and assumptions, as summarized in Table 1. Dimensioning and system sizing were determined by analyzing the company's daily production volume, the quantity of water content to be removed, the total thermal energy required to achieve the target moisture reduction, incident solar radiation on a horizontal surface, the drying period, and the operating temperature of both the product and the air stream. These conditions and assumptions were informed by findings from relevant literature (Rathore and Panwar, 2010; Mohana et al., 2020; Ortiz-Rodríguez et al., 2022) and the physical and chemical engineering properties of the material, form the basis for the theoretical design parameters summarized in Table 4.

Table 5
Final dimensions of drying chamber and drying product.

Scaled dimensions of the chamber and drying product			
Geometry	Dimension		
	Length *(m)*	Width *(m)*	Height *(m)*
Drying Chamber	0.35	0.2	0.1
Drying Product onFig. 4(b)	0.003	0.025	0.002
Drying Product onFig. 4(c)	0.24	0.04	0.002

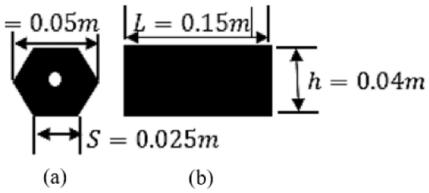

Fig. 3. Shape of the briquette, (a) face and (b) lateral surface area.

2.3.2. Description of the product to be dried

The proposed CFD model is versatile and designed to simulate the drying kinetics of various products with different geometries, shapes, and moisture content levels, allowing for optimization in diverse drying applications. In this study, the model is tailored for drying hexagonal-shaped charcoal briquettes produced from charcoal dust, with cassava flour used as a binder. The initial moisture content of these wet briquettes is approximately 50 % (wb), and the drying objective is to reduce this to 10 % (wb) to meet the quality standards required for storage and usage of the fuel. Each briquette's physical dimensions were used to determine the total area they occupy within the drying chamber, as shown in Table 2. This data is critical for modeling effective airflow and heat transfer across the drying product, ensuring an efficient and consistent drying process.

2.3.3. Arrangement of charcoal briquette

The arrangement of the briquettes inside the dryer was based on their shape, surface area, and the use of forced convection for heat transfer. The briquettes have a hexagonal shape with a circular orifice

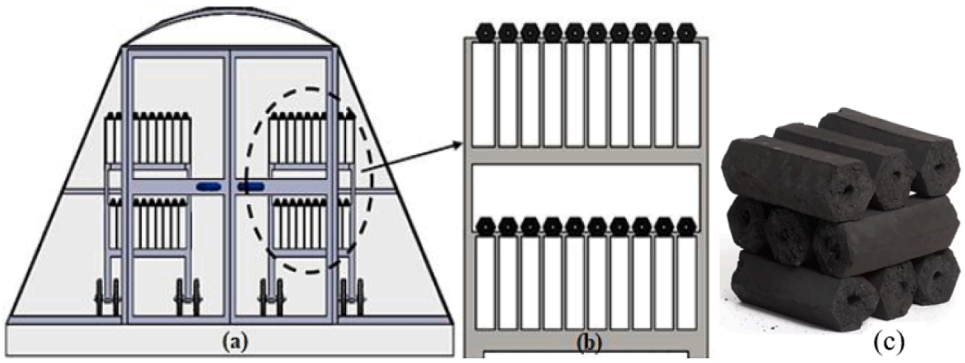

Fig. 4. Arrangement of charcoal briquette on beds (a) and (b), real shape of briquettes (c).

(1.5 cm diameter) in the center, as illustrated in Fig. 3(a) and 4(c). The drying chamber operates on the principle of forced convection, where a stream of heated air is introduced from the rear and flows towards the front, aided by the axial fans and the design of the drying beds (Fig. 1).

The arrangement of the briquettes within the solar tunnel dryer was optimized based on their hexagonal shape and the need for efficient airflow around each briquette. Each briquette includes a central circular orifice with a diameter of 1.5 cm, designed to improve air circulation and enhance drying efficiency by exposing the interior surfaces of the briquette to heated air. This configuration is shown in Figs. 3(a) and 4 (c). The drying process operates on the principle of forced convection, in which a stream of heated air is introduced from the rear of the drying chamber and directed toward the front by axial fans. This airflow design is facilitated by the layout of the drying beds, as illustrated in Figs. 1 and 4(a). To maximize heat transfer, the briquettes are arranged in an east-west orientation, optimizing surface exposure to the airflow and reducing heat transfer losses. Minimal contact with the support structures further enhances the drying process by reducing conductive heat losses to the drying bed frame.

Each drying bed is structured to hold approximately 800 briquettes, organized in two rows with ten columns, and spaced with a 2 cm gap between columns to ensure optimal airflow distribution. Additionally, the rows are elevated on a T-shaped frame structure (Fig. 4(b)), which supports the briquettes while allowing the hot air to flow freely around each one. This design ensures uniform exposure to the airflow, improving drying uniformity and efficiency across the batch. By integrating these arrangements and configurations, the model maximizes the airflow and thermal efficiency of the drying chamber, demonstrating its adaptability and potential application across various drying scenarios, especially for biomass products requiring high efficiency drying methods.

The frame structure within the drying chamber is essential for maintaining tension and support for the polyethylene cover, which captures solar thermal energy and ensures a stable solar collector area. After evaluating multiple designs (Zziwa et al., 2023; Bala and Debnath, 2012), a trapezoidal frame configuration was selected, as this orientation reduces shading in an East-West alignment, thereby maximizing solar radiation capture. This design enables approximately 95 % coverage of the collector surface area during daylight hours (Fig. 1). The frame incorporates ten support elements spaced 1.75 m apart, providing structural stability. Aluminum was chosen as the frame material due to its lightweight, durable, affordable properties, ease of welding, and high resistance to rust and corrosion, which is particularly beneficial in humid conditions, making it ideal for this solar drying application.

2.4. Moisture content analysis of charcoal briquettes

The drying process analysis for the charcoal dust briquettes produced by Verde Africa Ltd involved calculating both the initial and desired final moisture content to ensure efficient moisture removal under simulated drying conditions. The total daily production of wet charcoal briquettes was approximately 1120 kg, with an initial moisture content ($M_{i,wb}$) of 50 % on a wet basis. The target was to achieve a final moisture content ($M_{f,wb}$) of 10 % on a wet basis after drying.

2.4.1. Wet basis analysis

Moisture Content to be Removed ($M_{r,wb}$) on a wet basis was calculated as the difference between the initial ($M_{i,wb}$) and final ($M_{f,wb}$) moisture contents (Ekechukwu, 1999; Janjai et al., 2009):

$$M_{r,wb} = M_{i,wb} - M_{f,wb} \tag{1}$$

The initial mass of water content (m_{wi}) in the product before drying (m_{wi}) was determined by multiplying the total mass of the daily production (m_{bi}) by the initial moisture content:

$$m_{wi} = m_{bi} * M_{i,wb} \tag{2}$$

The total mass of solid charcoal dust (m_s) which represents the charcoal dust content, was determined by subtracting the initial mass of water from the total mass of the product:

$$m_s = m_{bi} - m_{wi} \tag{3}$$

2.4.2. Dry basis analysis

Calculations were also carried out on a dry basis to facilitate replication and standardize the results.

Initial Moisture Content in Dry Base ($M_{i,db}$):

$$M_{i,db} = \frac{M_{i,wb}}{100 - M_{i,wb}} * 100 \quad \% \tag{4}$$

Final Moisture Content in Dry Base ($M_{f,db}$):

$$M_{f,db} = \frac{M_{f,wb}}{100 - M_{f,wb}} * 100 \quad \% \tag{5}$$

Moisture Content to be Removed in Dry Base ($M_{i,db}$):

$$M_{r,db} = M_{f,db} - M_{i,db} \tag{6}$$

The total water to be removed (m_{wr}), based on the calculated moisture removal on a dry basis, was determined as the total mass of water required to be removed from the product:

$$m_{wr} = m_s * M_r \tag{7}$$

The final mass of the briquettes post-drying (m_{bf}), accounting for the removed water, is given by:

$$m_{bf} = m_{bi} - m_{wr} \tag{8}$$

Final Quantity of Water in the Product (m_{wf}): After drying, the remaining water content was:

$$m_{wf} = m_s * M_{f,db} = m_{bf} - m_s \tag{9}$$

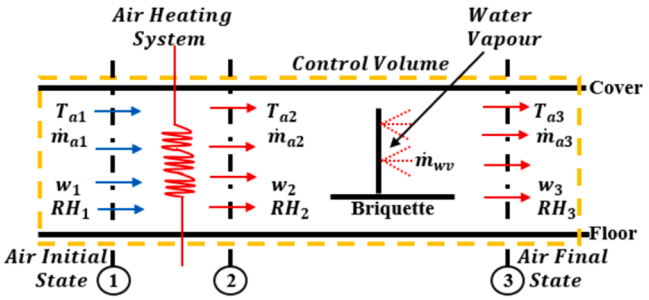

Fig. 5. Schematic diagram of the drying chamber with each process involved.

2.5. Thermal energy required for drying

The total heat energy required to dry the wet charcoal briquette to the target moisture content is a combination of the sensible heat of the charcoal dust (dry matter), the sensible heat of water in the briquette, and the latent heat needed to evaporate the water. This calculation considers available solar radiation as the primary energy source.

Sensible heat of charcoal dust in the product to raise the temperature of the dry matter within the briquettes ($Q_{s,b}$) is given by (Ekechukwu, 1999):

$$Q_{s,b} = m_s C_{pb}(T_b - T_i) \tag{10}$$

For sensible heat of water in the product, the energy needed to raise the temperature of the water content within the briquettes, ($Q_{s,w}$) is calculated as:

$$Q_{s,w} = m_{wi} C_{pw}(T_w - T_i) \tag{11}$$

Latent heat of water evaporation: the energy required to evaporate the water in the product ($Q_{l,w}$) is calculated as:

$$Q_{lw} = m_{wr} h_{fg} \tag{12}$$

Total thermal energy required (Q_t) for drying is the sum of all three components:

$$Q_t = Q_{s,b} + Q_{s,w} + Q_{l,w} \tag{13}$$

The thermal energy rate required during the drying period, ($\dot{Q}_r$) is defined by:

$$\dot{Q}_r = \frac{Q_t}{t_d} \tag{14}$$

Assumptions and Temperature Conditions.

To ensure accurate calculations, the following assumptions were made based on literature and typical ambient conditions in Maputo:

- Initial temperature of the charcoal dust and water ($T_{bi} = T_{wi} = T_i$) is 23 ℃, representing the average daily ambient temperature.
- Final drying temperature of the product ($T_b = T_w = T_f$) is set to 50 ℃, as recommended for optimal drying.

2.6. Psychometric analysis of drying chamber

Psychrometry, the study of thermodynamic properties of moist air, is essential for understanding the changes in air properties within the drying chamber(Ekechukwu, 1999). The analysis here assumes the drying chamber as a control volume and applies psychrometric principles specifically, the concepts of sensible heating and adiabatic humidification based on key air properties: temperature (T), mass flow rate ($\dot{m}_a$) specific humidity (w), and relative humidity (RT). These properties are monitored at three primary states within the drying process, outlined in Fig. 5.

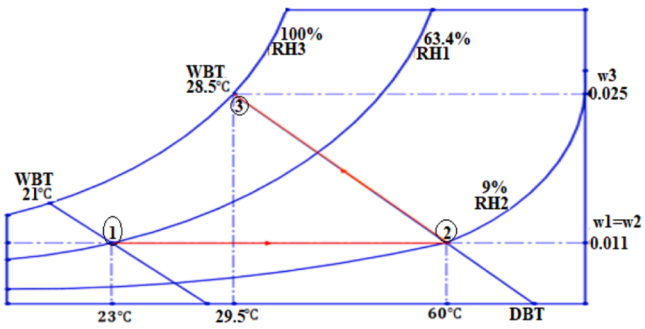

Fig. 6. Psychrometric chart illustrating adiabatic humidification in the proposed drying system.

2.6.1. Air heating and evaporation processes within the control volume

The control volume of the drying system comprises two main processes:

Air Heating System: This includes hot air from the Solar Air Heater (SAH) and the solar radiation trapped within the chamber.

Evaporation System: Water molecules within the charcoal briquettes evaporate as they gain heat from the convective hot air stream.

2.6.2. Key psychrometric states within the drying chamber

The air properties across the drying chamber vary between three primary states illustrated in Fig. 6:

State 1: Initial ambient air conditions, reflecting the annual average climate of Maputo, with a dry bulb temperature (*DBT*) of $T_{a1,\ d} = 23$ ℃ and relative humidity (*RH1*) of 63.4 %. From psychrometric charts, this yields a specific humidity (w_1) of 0.011 and a wet bulb temperature (*WBT*) ($T_{a1,w}$) of 21 ℃.

State 2: Post-sensible heating within the SAH. Here, the air stream reaches a *DBT* of $T_{a2} = 60$ ℃, with no moisture content change ($w_2 = w_1 = 0.011$). At this state, the relative humidity decreases to $RH_2 = 9$ and *WBT* increases to $T_{a2,w} = 28.5$ ℃.

State 3: After adiabatic humidification, where $T_{a3,w} = T_{a2,w} = 28.5$ ℃ and relative humidity reaches $RH3 = 100$. This process increases the specific humidity to $w_3 = 0.025$ and decreases the DBT to $T_{a3,d} = 29.5$ ℃.

Process (1–2): Sensible heating, where air temperature rise from 23 ℃ to 60 ℃, *WBT* increases from 21 ℃ to 28.5 ℃, relative humidity drops from 63.4 % to 9 %, and specific humidity remains constant.

Process (2–3): Adiabatic humidification, wherein *DBT* decreases from 60 ℃ to 29.5 ℃ and specific humidity rises from 0.011 to 0.025 while maintaining constant *WBT* at 28.5 ℃.

Process (1–3): Combined heating and humidification, resulting in an overall increase in *DBT*, *WBT*, relative humidity, and specific humidity across the drying chamber.

2.6.3. Mass flow rate estimation

2.6.3.1. Adiabatic humidification mass flow rate. The air mass flow rate ($\dot{m}_a$) is derived from the mass balance, considering the moisture carried by the air and evaporated from the product:

$$\dot{m}_a = \frac{\dot{m}_f}{(w_3 - w_2)} \tag{15}$$

Where $\dot{m}_f$ is the drying rate of the product given by:

$$\dot{m}_f = \frac{\dot{m}_{wr}}{(t_d)} \tag{16}$$

By substituting values, the equation yields the mass flow rate, $\dot{m}_a$ for adiabatic humidification.

2.6.3.2. Non-adiabatic humidification mass flow rate. The estimation of

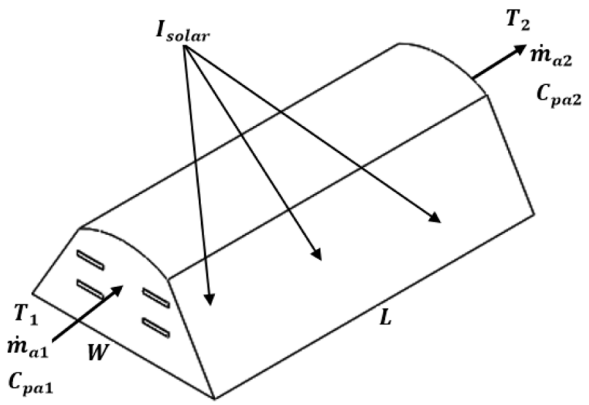

Fig. 7. Energy balance schematic of the solar tunnel dryer.

the air mass flow rate for non-adiabatic humidification, or sensible heating, is represented by the red line between State 1 and State 2 in Fig. 5. This calculation is based on the energy balance principle (Janjai et al., 2009), assuming the drying chamber as a control volume (CV). The incident solar radiation and the thermal energy of the air at both State 1 and State 2 are illustrated in Fig. 7.

$$E_{solar} = E_{air2} - E_{air1} \tag{17}$$

$$\eta I A_p = \eta I A_p = \dot{m}_{a2} h_2 - \dot{m}_{a1} C_{pa1} h_1 \tag{18}$$

The energy balance equation for the drying chamber is expressed as:

$$\eta I A_p = \dot{m}_a (h_2 - h_1) \tag{19}$$

where η is the system efficiency, I is the incident solar radiation, and A_p is the projected area receiving the radiation. Rearranging this equation allows for determining the air mass flow rate $\dot{m}_a$:

$$\dot{m}_a = \frac{\eta I A_p}{(h_2 - h_1)} \tag{20}$$

2.6.4. Governing equations

To model the airflow, heat transfer, and radiation effects inside the solar tunnel dryer for drying charcoal dust briquettes, several governing equations and specific simulation models were employed. The analysis integrates fluid flow, heat transfer, and species transport, with boundary conditions and solution methods set to reflect real drying chamber conditions. Below is an overview of the main models and equations used (Tuncer et al., 2020; Aukah et al., 2018).

2.6.4.1. Turbulence model. Realizable k - ε Model with Enhanced Wall Treatment: Given the forced convection in the drying system, a turbulent flow was induced due to high airflow rates. The Realizable k - ε model, which includes transport equations for turbulent kinetic energy (k) and its dissipation rate (ε) was selected for its accuracy in complex flow fields and its efficient computational demands. Enhanced wall treatment improves near-wall predictions, critical for heat transfer

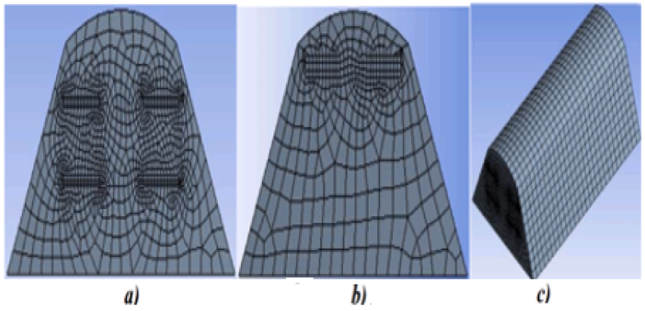

Fig. 9. Meshing of Model 1. Face mesh (a), back mesh (b), and 3D mesh (c).

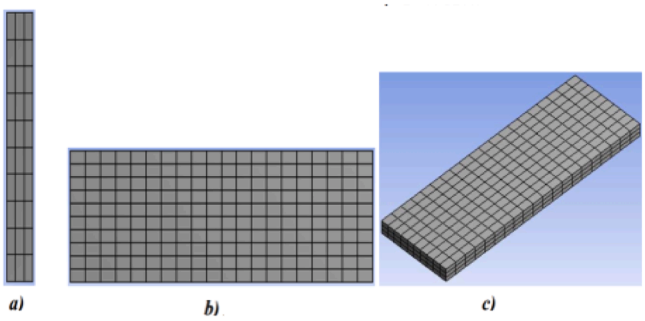

Fig. 10. Meshing of Model 2. Face mesh (a), back mesh (b), and 3D mesh (c).

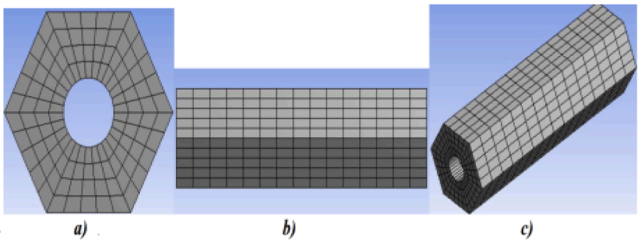

Fig. 11. Meshing of Model 3, (a) Face mesh, (b) side mesh, and (c) 3D mesh.

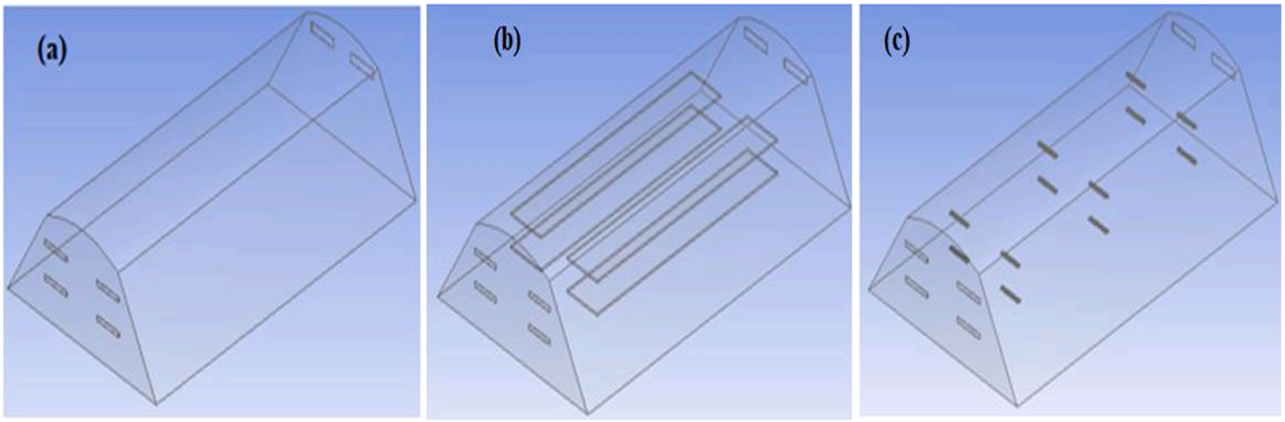

Fig. 8. Drying chamber models: (a) Control dryer without product, (b) Dryer with complete product representation, (c) Dryer with select product samples.

interactions within the chamber.

Governing equations for the k - ε model:

Turbulent Kinetic Energy (k) Equation

$$\rho\frac{\partial k}{\partial t}+\rho u.\nabla k=\nabla.\left[\left(\mu+\frac{u_t}{\sigma_k}\right)\nabla k\right]+G_k+G_b-\rho\varepsilon-Y_M+S_k \quad (21)$$

Dissipation Rate (ε) Equation,

$$\rho\frac{\partial k}{\partial t}+\rho u.\nabla\varepsilon=\nabla.\left[\left(\mu+\frac{u_t}{\sigma_\varepsilon}\right)\nabla\varepsilon\right]+C_{1\varepsilon}\ \frac{\varepsilon}{k}(G_k+C_3\varepsilon G_b)-C_{2\varepsilon}\frac{\varepsilon^2}{k}+S_\varepsilon \quad (22)$$

Radiation Model.

Discrete Ordinates (DO) Radiation Model: The solar radiation within the dryer depends on location, time, and seasonal variation. The DO model solves the radiative transfer equation (RTE) for discrete solid angles and provides accurate calculations of irradiance at semi-transparent walls. Solar radiation was simulated using parameters specific to Maputo (latitude: −26°, longitude: 32.6°) and for two representative days with maximum and minimum solar radiation.

2.6.4.2. Governing equation for radiative heat transfer

$$\nabla.(q_r)+a\sigma T^4=\int I(r,s)d\Omega \quad (23)$$

Species Transport Model:

The simulation involved a mixture of dry air and water vapor to account for the humid air inside the drying chamber. Species transport was activated to maintain constant mass fractions of dry air and water vapor, with no moisture transfer between the briquettes and the moist air (adiabatic drying assumption).

2.6.4.3. Governing equation for species transport

$$\nabla.(\rho u.Y_i)=-\nabla.J_i+R_i+S_i \quad (24)$$

where Y_i is the mass fraction of species i, and J_i represents the diffusion flux. These equations were utilized.

2.7. ANSYS fluent simulation of STD

2.7.1. Geometry creation

The geometric dimensions of the solar tunnel dryer (STD) were scaled down to facilitate meshing and computational iterations, with adjustments including a 20 % reduction in the width and height of the frontal surface and a 50 % reduction in the length of the lateral surface. The scaled dimensions of the dryer are detailed in Table 4. For the simulation, three models were created using SOLIDWORKS 2018 and imported into ANSYS Fluent 19.2 to analyze temperature, velocity, and pressure distributions inside the chamber. Inlet and outlet apertures were consistent across all models, with four inlets (0.03 m in length, 0.0042 m in height) for heated air and two outlets (0.03 m in length, 0.0084 m in height) for humid air exhaust. Fig. 4 illustrates the 3D geometries of the chamber, both with and without the drying product.

Model 1 (Fig. 4a) represents the proposed solar tunnel dryer without any drying product, serving as the baseline configuration for assessing the distribution of temperature, velocity, and pressure within the chamber. The data from this model will be used as a reference for comparing the performance of alternative configurations. They can also be applied to investigate the drying kinetics of various products under similar drying conditions.

Model 2 (Fig. 4b) includes a representation of the drying product, which has been simplified into a rectangular shape to preserve the same heat transfer surface area. This adjustment addresses challenges related to meshing complexity, thereby improving the accuracy of the CFD simulations while ensuring consistency in the heat exchange process.

Model 3 (Fig. 4c) incorporates the solar tunnel dryer with actual samples of the drying product, specifically 120 charcoal briquettes arranged in 12 rows. These briquettes, modeled in their real shapes, are positioned in both drying beds' front, middle, and back layers to simulate realistic drying conditions more closely and provide a comprehensive understanding of airflow and temperature distribution during the drying process.

All three models share the same inlet and outlet specifications, with four hot air inlets (0.03 m in length, 0.0042 m in height) for heated air entry and two outlets (0.03 m in length, 0.0084 m in height) for the exhaust of humid air. Table 4 provides detailed dimensions for each component used in the simulation. The next step in the process involves mesh generation for CFD analysis.

2.7.2. Mesh development

Mesh generation was conducted following the creation of each model geometry and the definition of fluid and solid domains using the Design Modeler module. The Linear Hex Dominant meshing method was employed to ensure precise results, with all elements set to Quad. This configuration enhances the accuracy of the simulation by improving the resolution of key flow and heat transfer regions, especially around the boundaries where significant gradients in temperature and velocity occur. Special attention was paid to the inlets, outlets, and the interaction between the drying product and airflow to ensure proper representation of convective heat transfer mechanisms.

Edgy sizing and face meshing techniques were applied to reduce the element and node count while improving element profiles. This optimization aimed to enhance convergence rates and achieve more accurate simulation results across all models.

Model 1 Meshing.

Four different edgy sizing settings were applied based on element length to further refine the element profiles. Additionally, face meshing was applied to the top and bottom surfaces of the model to ensure smoother transitions in critical regions. The final mesh configuration yielded element dimensions of 0.002 m, resulting in a total of 13,916 elements and 11,758 nodes. The maximum skewness value was 0.99994, indicating acceptable element quality for simulations (Fig. 5).

The air domain in Model 1 was bounded by several heat transfer surfaces, including 4 inlets, 2 outlets, 5 cover walls, and 1 floor wall. These boundary conditions play a critical role in accurately simulating the convective and radiative heat transfer processes within the drying system, ensuring that airflow and temperature distribution inside the chamber are properly modeled.

Model 2 Meshing.

In Model 2, the meshing process focused on both the air domain of the drying chamber and the solid domains representing the modified drying product, which were characterized by rectangular geometry. Heat transfer surface boundaries were defined throughout the system. The element profiles for the rectangular drying product were refined using three distinct edgy sizing configurations along each edge, based on their respective lengths. This refinement ensured a higher degree of mesh resolution and accuracy, particularly for capturing the heat transfer and airflow interactions.

The mesh editing techniques applied to the air domain in Model 2 were consistent with those used in the previous models, maintaining methodological uniformity and ensuring a reliable basis for comparative analysis across the simulations. Following the mesh refinement of the drying product, the final element size measured 0.004 m, with a total of 20,800 elements and 27,848 nodes. The overall Model 2 configuration included 34,716 elements and 38,606 nodes, achieving a maximum skewness value of 0.99978. Heat transfer boundaries included 4 inlet surfaces, 2 outlet surfaces, modified briquette walls (front, back, top, and bottom), 5 cover walls, and 1 floor wall, providing a comprehensive mesh structure for the accurate simulation of airflow and heat transfer processes.

Model 3 Meshing.

For Model 3, the meshing approach focused on the air domain geometry of the drying chamber and the solid domain of the charcoal dust

Table 6
The Summary of Operating Condition.

Summary of Operating Conditions	
Operating Conditions	**Governing Equation**
Solver	3D Simulation Implicit Formulation Pressure Based Absolute Velocity Formation Steady State Analysis
Gravity	$-9.81 m/s^2 \ldots Y - axis$
Energy Equation	On
Viscose Model	Realizable k–ε Model Enhanced Wall Treatment
Radiation Model	Discrete Ordinate (DO)
Species Transport	On

briquettes, which were represented with their actual geometric attributes. The heat transfer surface boundaries were applied across the entire system. Refinement of the drying product's element profile involved utilizing two distinct edgy sizing techniques based on their length, along with face meshing applied to both the front and back surfaces of the model. Following optimization, the mesh for the drying product achieved an element size of 0.005 m, comprising a total of 216,000 elements and 288,000 nodes, with a maximum skewness of 0.99983. The entire Model 3 consisted of 229,916 elements and 299,758 nodes. Heat transfer surface boundaries included 4 inlet surfaces, 2 outlet surfaces, all surfaces of the briquette walls (including both outer and inner hole surfaces), 5 cover walls, and 1 floor wall.

2.7.3. Simulation setup

2.7.3.1. Operating conditions. Turbulence Model: The Realizable k-ε turbulence model, enhanced with Enhanced Wall Treatment, was selected for simulating complex airflow fields within the drying chamber (Table 6). This model is particularly suitable due to its accurate prediction of spreading rates, high convergence, and low computational demands. Its proven ability to simulate robust flow dynamics within similar systems, along with its compatibility with the drying chamber, justifies its selection (Aukah et al., 2018; Mehdipour and Ghaffari, 2021). Top of Form

Radiation Model: The Discrete Ordinates (DO) radiation model was employed to account for the intricate factors affecting solar radiation, including time of day, geographical location, and weather conditions. This model solves the radiative transfer equation (RTE) by dividing the domain into discrete solid angles and calculating irradiance at semi-transparent walls (Duong et al., 2021; Gunnarsson et al., 2020)). Mozambique's geographical parameters (longitude: 32.6°, latitude: 26°, GMT +2) and local weather conditions in Maputo City were applied. The mesh orientation aligns North with the negative X-direction and East with the positive Z-direction to simulate solar radiation effects accurately.

Species Transport**:** The simulation considers heat transfer only, without mass transfer modeling. Thus, moisture transfer between the drying product and moist air is not modeled, and the mass fraction of moist air remains consistent throughout the system. The moist air entering the chamber was set at a mass fraction of 0.0101.

2.7.3.2. Boundary conditions. Specific boundary conditions were established for each model to simulate thermal exchange within the drying chamber accurately and tailored to their unique thermal properties and configurations. For Models 2 and 3, these conditions include the inlets, outlets, briquette walls, cover walls, and floor walls, each defined by distinct thermal properties (Table 7). Model 1 focuses solely on airflow without briquettes, thus excluding the briquette wall in its boundary definition. These customized parameters ensure a detailed and precise representation of heat transfer dynamics within the solar tunnel dryer.

2.7.3.3. Solution method. The simulation utilized the Pressure-Velocity Coupling method across all models to ensure accurate analysis of flow and thermal interactions. For spatial discretization, the following methods were applied: Second Order for pressure analysis, Second Order Upwind for momentum, energy, and water vapor (H_2O), and First Order Upwind for turbulent kinetic energy and turbulent dissipation rate. These methods provide an optimal balance between computational efficiency and accuracy in capturing the dynamics within the drying chamber.

3. Results and discussions

3.1. Simulation results: general trends and implications

The simulation results underscore the potential of the solar tunnel dryer as an efficient solution for biomass drying in regions with significant solar energy potential. The findings reveal notable improvements in thermal performance, air distribution, and drying efficiency. These advancements are essential for promoting sustainable drying technologies, especially in regions that are heavily reliant on biomass fuels for energy. The results show a strong correlation between solar radiation

Table 7
Summary of boundary conditions.

Summary of Boundary Conditions				
Boundary Conditions	**Parameters**	**Values**	**Material**	**Source**
Inlet	Mass Flow Rate Temperature Mass Fraction		Moist Air	User-defined
Outlet	Pressure Outlet Mass Fraction	0 0	Moist Air	User-defined
Briquette-Wall	Wall Thickness Emissivity Absorptivity H	$0.002m$ 0.96 0.80 $13.9 W/m^2 \bullet K$	Charcoal Dust Briquette	User-defined
Cover -Wall	Wall Thickness Emissivity Absorptivity H	$0.0002m$ 0.94 0.02 $13.9 W/m^2 \bullet K$	Semi-Transparence Polyethylene	Monish et al. (2018b) Rathore and Panwar (2010) Balocco et al. (2018)
Floor-Wall	Wall Thickness Emissivity Absorptivity H	$0.015m$ 0.92 0.65 $13.9 W/m^2 \bullet K$	Concrete	User-defined

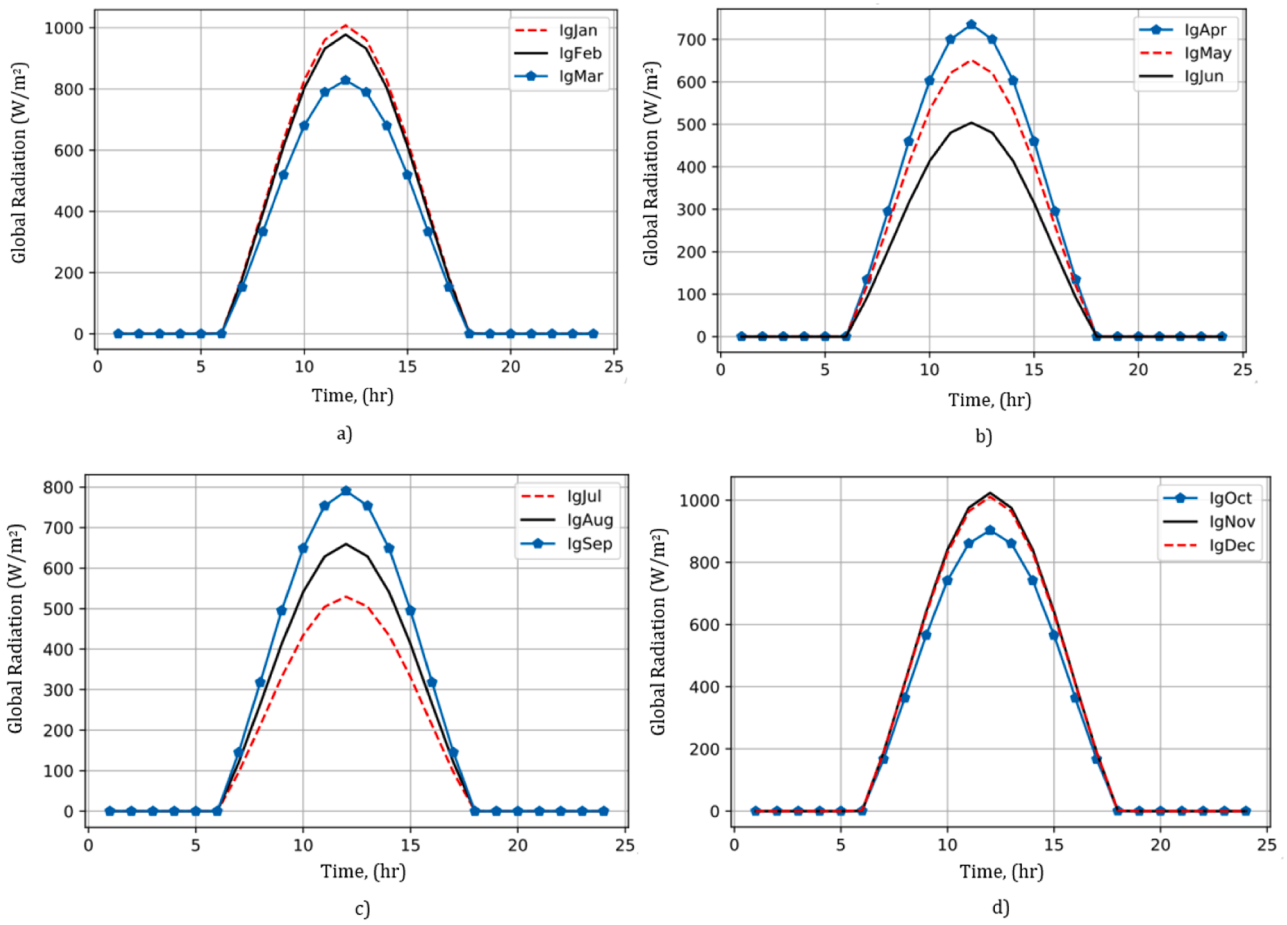

Fig. 12. Hourly Global Radiation Variation.

and the performance of the dryer, with peak efficiency observed during months with high solar radiation. Seasonal and hourly variations in solar radiation significantly influence temperature distribution, velocity profiles, and pressure within the drying chamber.

In Mozambique, where energy access is limited, and biomass fuels play a critical role, these improvements translate into practical benefits. For example, the simulations predict up to a 40% reduction in drying time during peak solar months, with substantial energy savings compared to traditional drying methods. This efficiency enhancement is vital in alleviating energy constraints, reducing deforestation, and improving economic outcomes for local communities.

3.1.1. Simulation results

This study evaluates the solar tunnel dryer (STD) performance under diverse conditions using computational fluid dynamics (CFD). The analysis focuses on temperature, velocity, and pressure distributions, with simulations conducted under varying solar radiation scenarios to reflect seasonal changes.

3.1.2. Estimation of hourly solar radiation

The monthly average hourly global, beam, and diffuse radiation data used for the mathematical modeling of the SAH and the CFD simulations of the STD were estimated using the Angstrom-Prescott empirical model. Solar radiation predictions were derived from monthly average daily sunshine hours for Maputo, based on 2022 NASA data. The results are presented in Fig. 12, which consists of four subfigures labeled as (a), (b), (c), and (d), illustrating the hourly variation of global radiation for different months of the year. Subfigure (a) shows the hourly variation of global radiation for January, February, and March. The data indicates a consistent trend with peak radiation occurring around noon, reflecting the relatively high solar intensity typical of early-year months in Maputo. Subfigure (b) presents the data for April, May, and June, highlighting a marked reduction in solar radiation, particularly in June, where the maximum global radiation recorded was 503.98 W/m^2 at noon and the minimum was 91.6 W/m^2 at 7 AM. Subfigure (c) covers the months of July, August, and September, showing a gradual increase in solar radiation as the transition toward sunnier conditions progresses, with notable midday peaks. Subfigure (d) provides the results for October, November, and December, with November standing out as the month with the highest recorded global radiation, reaching 1023.55 W/m^2 at noon and a minimum of 188.33 W/m^2 at 7 AM.

The results demonstrate that the highest global radiation level consistently occurs between 11 AM and 1 PM, irrespective of the month, while the lowest values are recorded at night. Seasonal variations are evident, with radiation levels peaking in November and declining significantly in June. This detailed analysis provides a clear understanding of the hourly and seasonal solar radiation variations critical for optimizing the performance of the proposed solar dryer.

3.1.3. Hourly temperature variation

MATLAB simulations were performed over 24 h on representative days for each month to analyze hourly fluctuations in the exit air temperature at the collector outlet. A constant air mass flow rate of 1.3572 kg/s was applied, with a time step of 60 s per iteration. The initial conditions for the simulation were set as follows: plate temperature $Tp = Tam + 1$, outlet air temperature $Tao = Tam + 0.5$, glass cover temperature $Tg = Tam + 0.25$, and inlet air temperature $Tai = Tam$. The simulation ran for 10,000 iterations.

The simulation results of the Solar Air Heater (SAH) reveal that the highest outlet air temperature occurs in November, reaching

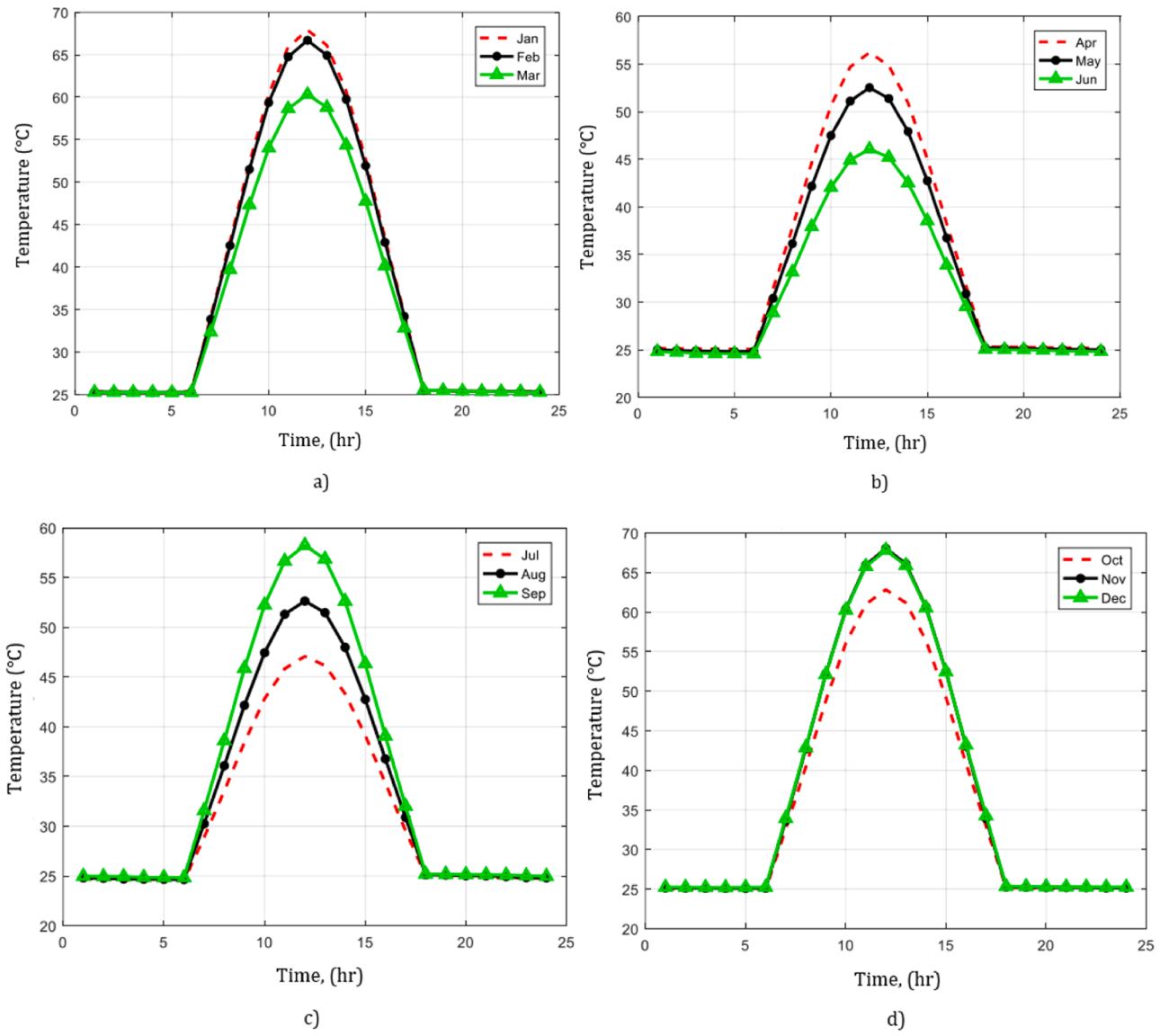

Fig. 13. Hourly exit air temperature variation.

approximately 68 °C, as illustrated in Fig. 13d, while the lowest is observed in June at around 46 °C, shown in Fig. 13b. Across the year, the collector outlet air temperature exhibits a seasonal trend, with values decreasing from the peak in November to the lowest in June before gradually increasing again. During five months of the year, as shown in Figs. 13a to13c, the outlet air temperature remains above 60 °C for several hours each day, whereas in October, represented in Fig. 13d, this duration is notably shorter. Conversely, the temperature remains consistently below 50 °C for the entirety of June and July, as depicted in Figs. 13b and 13c, highlighting the reduced solar radiation and ambient temperatures during these months.

3.2. ANSYS simulation results for model 1

The simulation analysis for Model 1 (drying chamber without charcoal dust briquettes) was conducted exclusively for periods of peak solar radiation in November and the lowest solar radiation in June. This section discusses the hourly average temperature variations, velocity vectors, streamlines, velocity contours, and pressure contours for November, along with temperature contours for both November and

Table 8
Hot Air Inlet Temperature and Diffuse Radiation on November 14th.

Inlet Temperature and Diffuse Radiation on November 14												
	AM						**PM**					
Time *(hr)*	**7**	**8**	**9**	**10**	**11**	**12**	**1**	**2**	**3**	**4**	**5**	**6**
HAIT (℃)	33.7	42.85	52.3	60.5	66.1	68.2	66.3	60.8	52.6	43.2	34.1	25.6
DR (W/m^2)	120	230	320	390	440	450	441	192	324	231	123	1

HAIT = Hot Air Inlet Temperature and DR = Diffuse Radiation

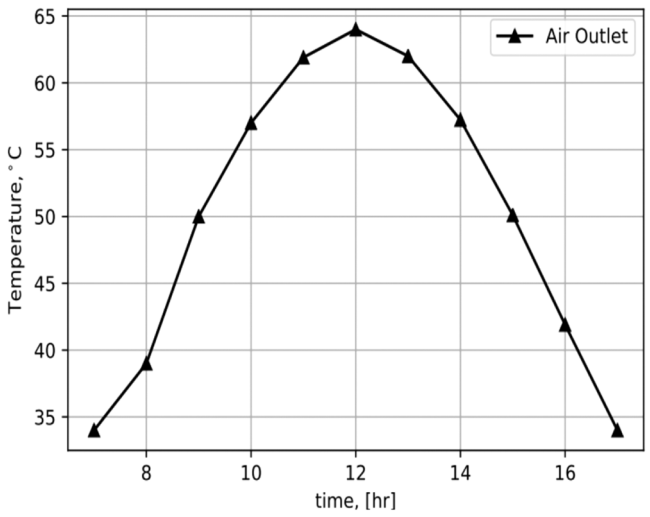

Fig. 14. Hourly variation of outlet air temperature.

June. The simulated air temperature at the SAH outlet was used as input for the STD, while the estimated diffuse radiation was used in the radiation model analysis. The input parameters are detailed in Table 8.

The hourly air temperature at the STD outlet was determined through a series of simulations conducted over 12 daylight hours. Fig. 14 graphically represents the simulation results, showing the hourly temperature variation at the drying chamber outlet. It illustrates the influence of solar radiation and inlet temperature on the outlet temperature. The results indicate that the maximum outlet temperature reaches 64 °C at noon, while the minimum is 26.82 °C at 6 PM. The outlet air temperature exceeds 50 °C for 7 h of the day. The temperature rises from sunrise, peaks midday, and declines until sunset.

Fig. 15 visually represents the simulation results, showing hourly temperature variations within the air domain at the central plane of the STD throughout the day. The distribution of temperature across the plane is influenced by solar radiation, considering the geographical location and the orientation of the drying chamber. The color gradient in the figure highlights temperature differences, with red representing the highest values and dark blue the lowest. Intermediate temperatures are denoted by shades of green, yellow, and orange, illustrating the system's thermal dynamics. This figure includes 12 images, each corresponding to a specific hour between 7 AM and 6 PM, showing how temperatures evolve.

The simulation results indicate a generally consistent temperature distribution across the central plane of the STD. Higher temperatures are observed on the southern side of the dryer, influenced by the East-West orientation of the system and its location south of the equator (Zziwa et al., 2023). From 9 AM to 3 PM, peak temperatures are concentrated in the center of the plane, gradually decreasing toward the cover and floor wall boundaries. Outside of these peak hours, the highest temperatures shift towards the floor wall, with a corresponding decrease toward the cover wall.

3.2.1. *Temperature profile*

Fig. 16 illustrates the air temperature distribution within the

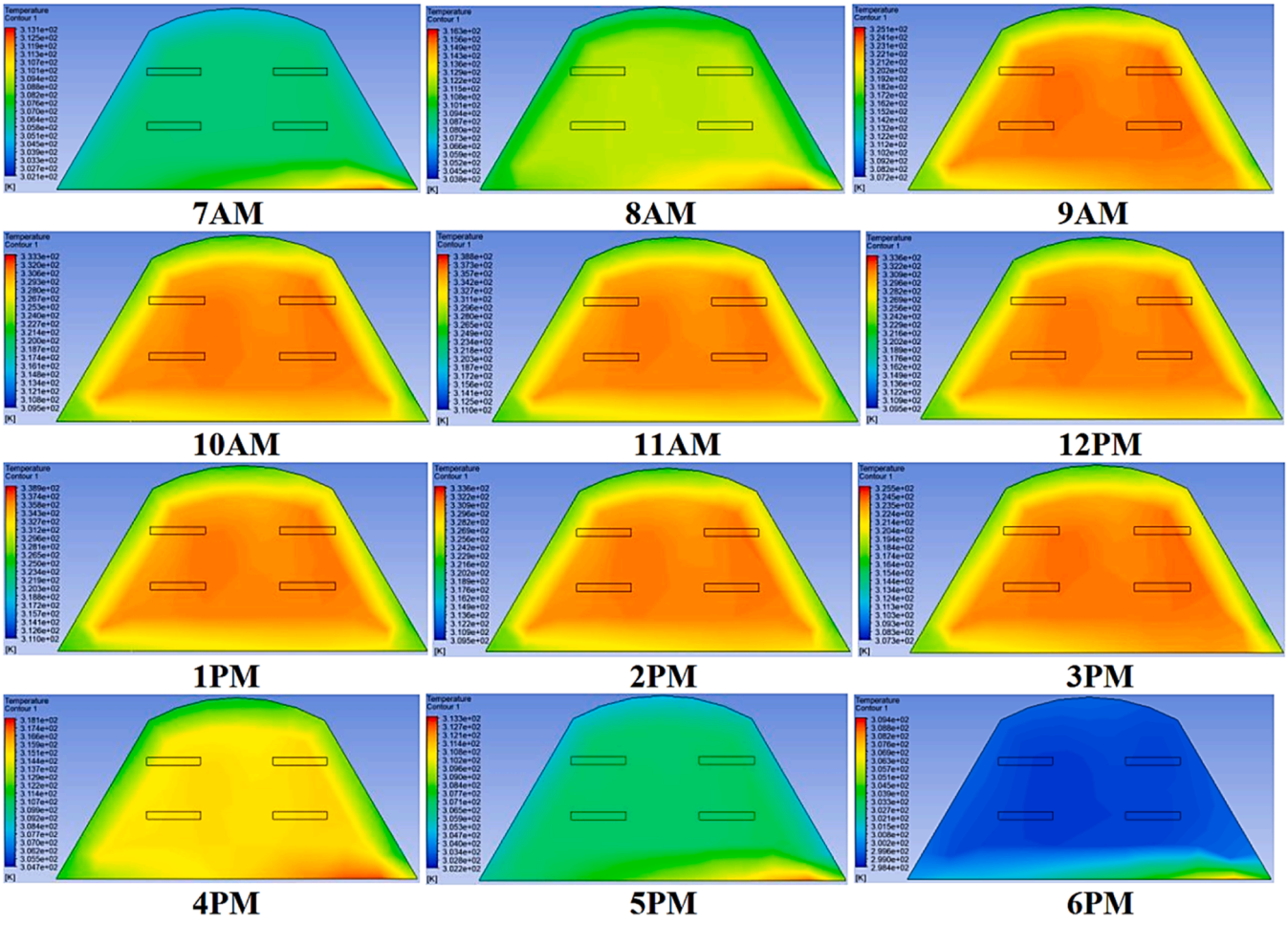

Fig. 15. Hourly temperature variation of air.

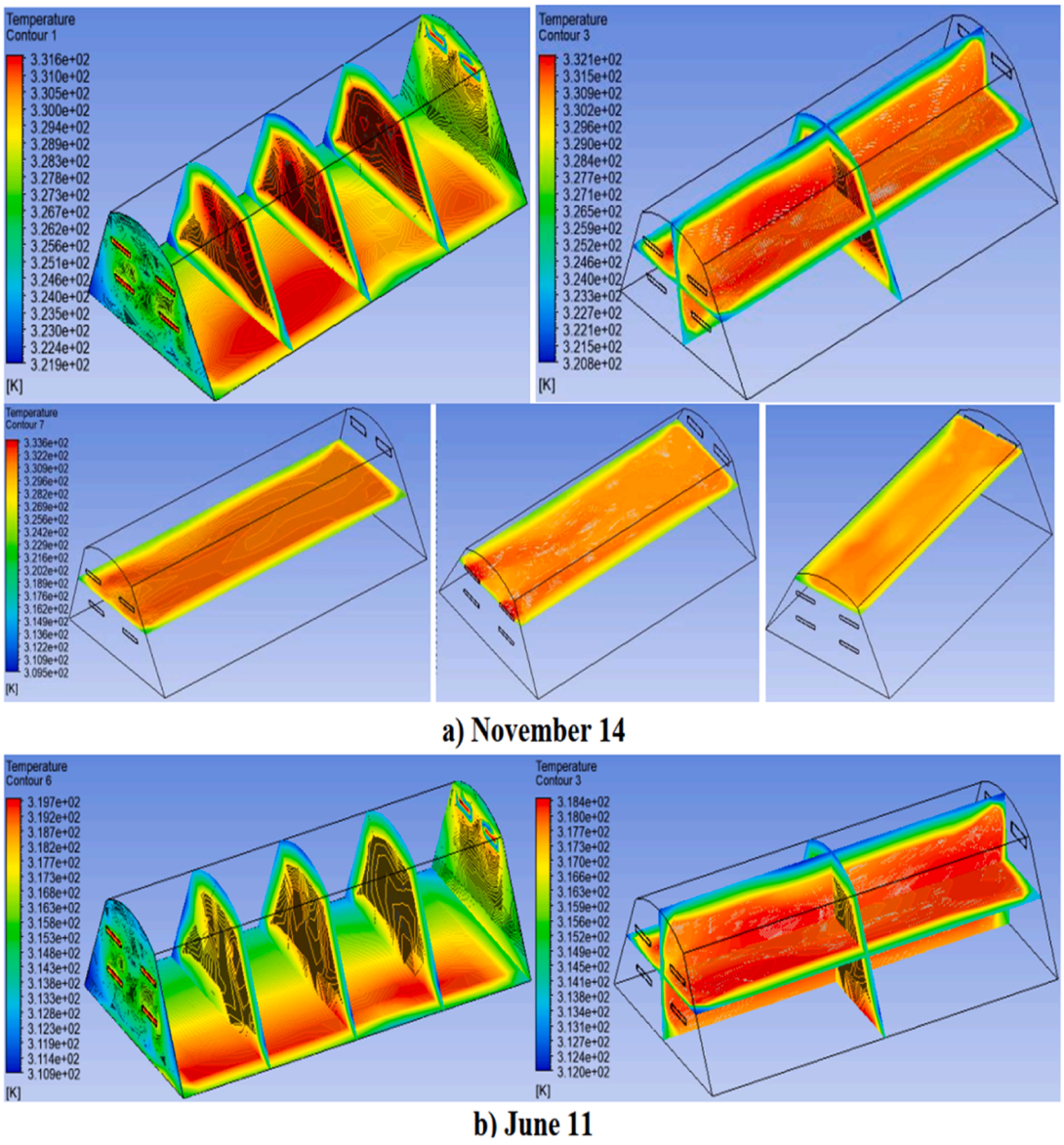

Fig. 16. Simulation result of temperature on a) November 14th and b) June 11th.

chamber for November 14th and June 11th. In June, the input parameters included an inlet air temperature of 46.22 °C and diffuse radiation of 170 W/m^2 at noon, while the parameters for November are detailed in Table 7. A constant inlet mass flow rate of 1.35720 kg/s was applied uniformly to each of the four inlets. The highest air temperature was observed in November, with the lowest in June, reflecting seasonal variations in solar radiation and inlet temperatures. The temperature profile indicates a more uniform distribution along the floor wall in November. Additionally, the results reveal nearly uniform temperature distribution along the face and back walls for both months, corroborating previous findings by Monish et al. (2018a) and Tran et al. (2021).

Fig. 17 illustrates the temperature variation of air within the STD along different axes: North-South, East-West, Top-Bottom, and Inlet-Outlet. Graphs (a), (b), and (c) are based on temperature measurements along straight lines passing through the center of the drying chamber, while graph (d) represents data obtained from an inclined line extending from the center of the inlet to the center of the outlet. The results indicate that air temperature is higher at the center of the drying chamber compared to the walls. In the North-South direction (graph a), temperature is higher near the south wall and lower near the north wall, a phenomenon attributed to the solar orientation of the site, where sunlight on the horizontal surface tilts towards the north. Along the East-West axis (graph b), the air temperature is higher near the west wall and lower near the east wall, influenced by airflow dynamics; higher velocity near the east wall reduces thermal diffusion, while lower velocity near the west wall leads to increased thermal accumulation due to turbulence effects. In the Top-Bottom axis (graph c), the air temperature is higher near the bottom (floor wall) compared to the top (cover wall), owing to the higher absorptivity and thermal conductivity of the floor wall, in contrast to the cover wall's lower absorptivity and higher transmissivity, which promotes heat dissipation. For the Inlet-Outlet axis (graph d), air temperature is highest at the inlet and gradually decreases towards the outlet, a result of thermal losses to the surrounding environment and through the boundary walls, particularly the cover wall.

3.2.2. *Velocity and pressure profile*

The Fluent simulation was initialized using input parameters such as temperature and diffuse radiation, as detailed in Table 7, for noon on November 14th. A constant inlet mass flow rate of 1.35720 kg/s was applied to each of the four inlets. The resulting velocity and pressure variations, along with their distribution, are shown in Fig. 18. Additionally, velocity streamlines are presented in Fig. 19, and velocity

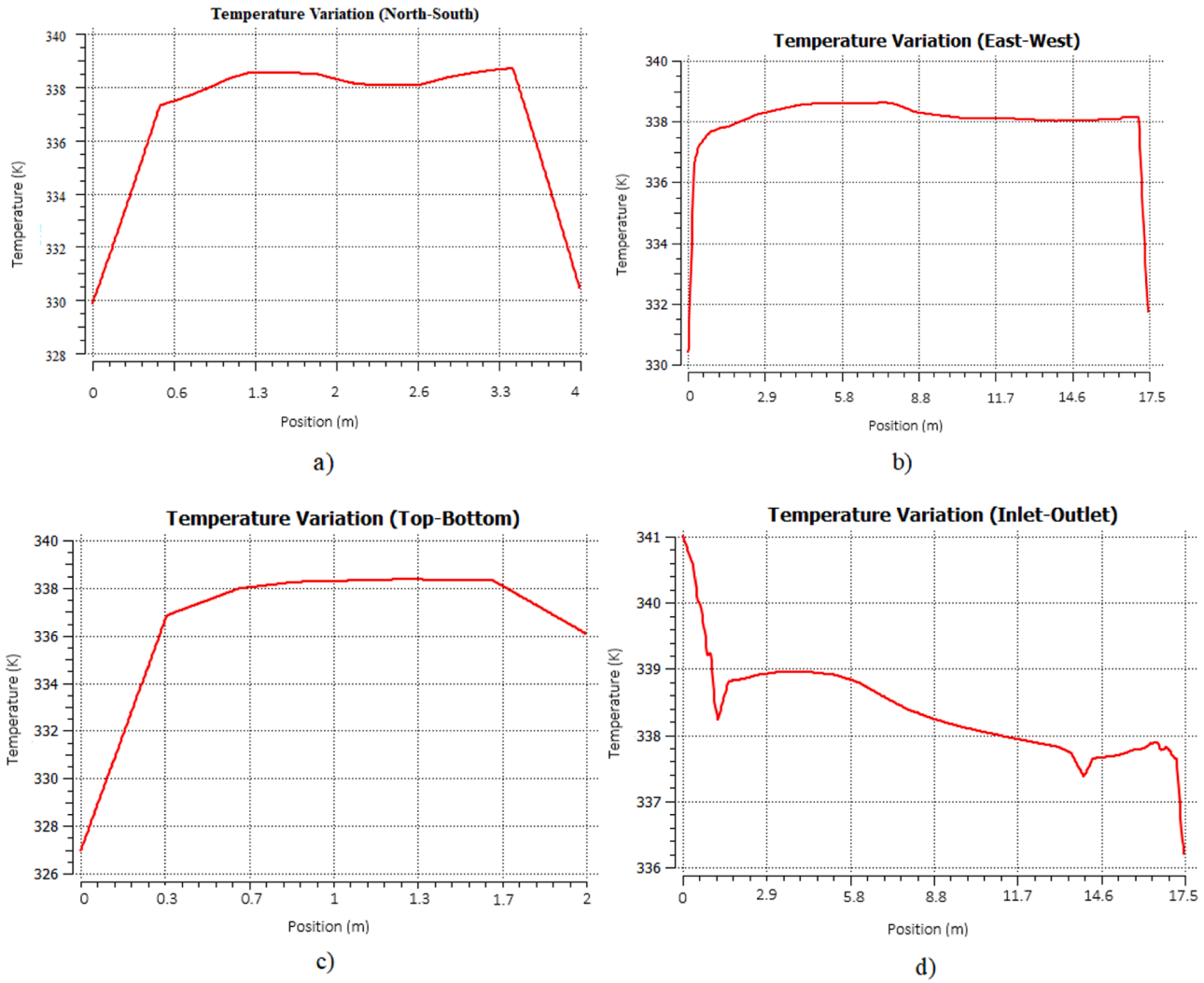

Fig. 17. Temperature variation inside the solar tunnel dryer at different positions on November 14th.

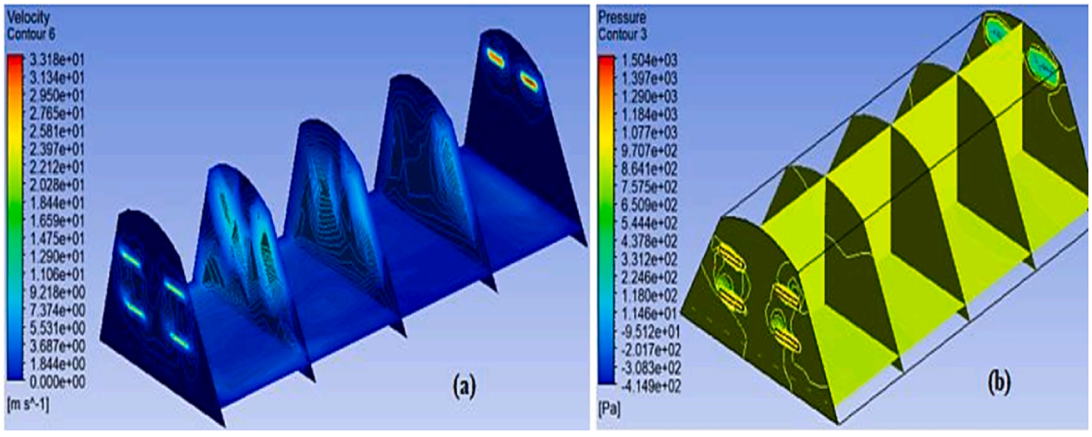

Fig. 18. Contour profile of velocity (a) and pressure (b).

vectors are illustrated in Fig. 21d.

The simulation results indicate a maximum velocity of 33.5 m/s at the outlet section, with a minimum velocity of 0 m/s near the solid wall boundaries. The average velocity within the drying chamber is 6.93 m/s. For pressure, the maximum value is 1521 Pa at the inlet, and the minimum value is −414.85 Pa at the outlet, with an average chamber pressure of 852.41 Pa. These values are consistent with the results of Monish et al. (2018a) and Tran et al. (2021), although discrepancies in the extreme values may be attributed to differences in the inlet mass flow rates, as well as variations in the dimensions, shapes, sizes, and positions of the air inlet and outlet sections across different models. Fig. 19 provides 3D, top, right-side, and front views of velocity

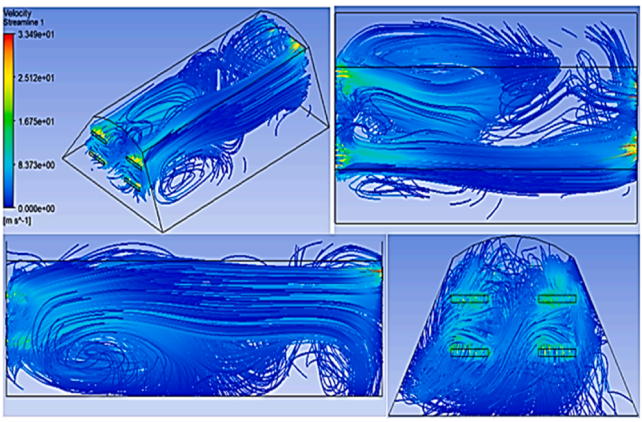

Fig. 19. Velocity Streamline of Model 1.

streamlines in the drying chamber, based on simulations from November 14th and June 11th.

The velocity streamline analysis shows higher turbulence around the inlet and outlet sections, a result of higher velocities and differences in cross-sectional areas. In contrast, lower turbulence is observed in other regions of the chamber, due to velocity and pressure drops near the solid boundary surfaces, particularly along the cover and floor inner walls. The pressure drop observed in the current analysis can be attributed to the high viscosity of air near solid boundaries, which suppresses turbulence in these areas. This aligns with findings by Patel and Patel (2014), who reported that pressure loss significantly impacts system efficiency. Patel emphasized the need for design modifications to minimize pressure drop and maximize output. The insights from both the analysis and literature suggest that optimizing the design to reduce pressure drop could enhance the efficiency of the solar tunnel dryer.

3.3. ANSYS Simulation results for model 2

3.3.1. Temperature profile

The Fluent simulation for Model 2 was initialized using input parameters of a hot air inlet temperature of 68 °C and diffuse radiation of 450 W/m^2 at noon on November 14th. The hot air inlet mass flow rate was kept constant at 1.35720 kg/s for each of the four inlets.

The temperature profiles within the chamber are illustrated in Fig. 20, which provides views of the temperature distribution: (a) across the briquettes, (b) at the center of the chamber on the z-x plane, (c) at the center on the x-y plane, and (d) at the center on the z-y plane.

The simulation results show that the maximum briquette temperature reached 57 °C on the upper bed of the left drying bed, while the minimum temperature was 49 °C on the lower bed of the right drying bed. The average surface temperature of the briquettes was recorded at 52 °C. Inside the chamber, temperatures ranged from a maximum of 65 °C at the inlet to a minimum of 36 °C at the outlet, with an average temperature of 58.5 °C across the chamber.

Fig. 20 reveals an almost uniform temperature distribution across the surface of the briquettes beneath both drying beds, with higher temperatures on the left (north-facing) side and lower temperatures on the right (south-facing) side. Additionally, uniform temperature distribution was observed in the chamber between the drying beds at the center (Fig. 20d), below the lower beds, and above the upper beds (Fig. 20c). Generally, the temperature variations within the chamber and on the briquette surface, highlight higher values near the inlet due to its north-facing orientation, while lower values are observed near the outlet. This difference is attributed to the air-solid interaction inside the chamber and the shading effect from the left drying bed on the right side (Rathore and Panwar, 2010).

3.3.2. Velocity and pressure profile

The Fluent simulation for Model 2 was initialized with a hot air inlet temperature of 68 °C, diffuse radiation of 450 W/m^2 at noon on November 14th, and a constant inlet mass flow rate of 1.35720 kg/s for

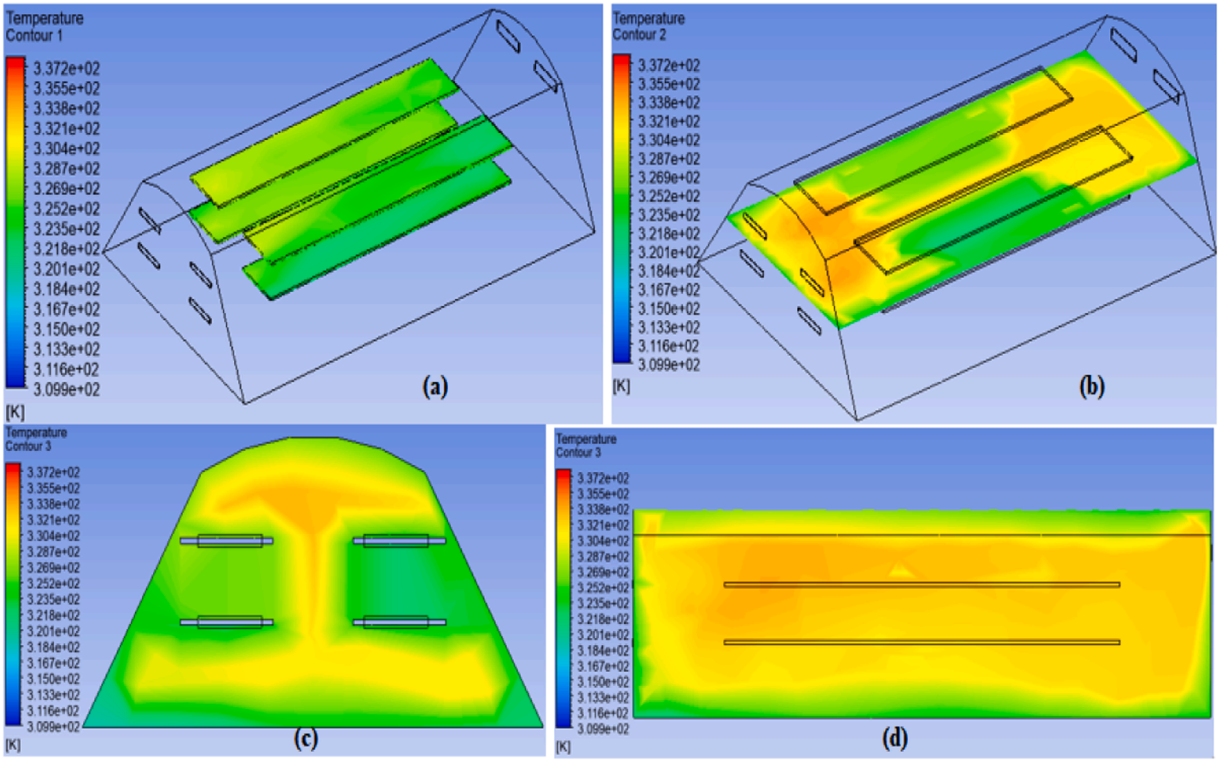

Fig. 20. Temperature profile of briquette wall and drying chamber.

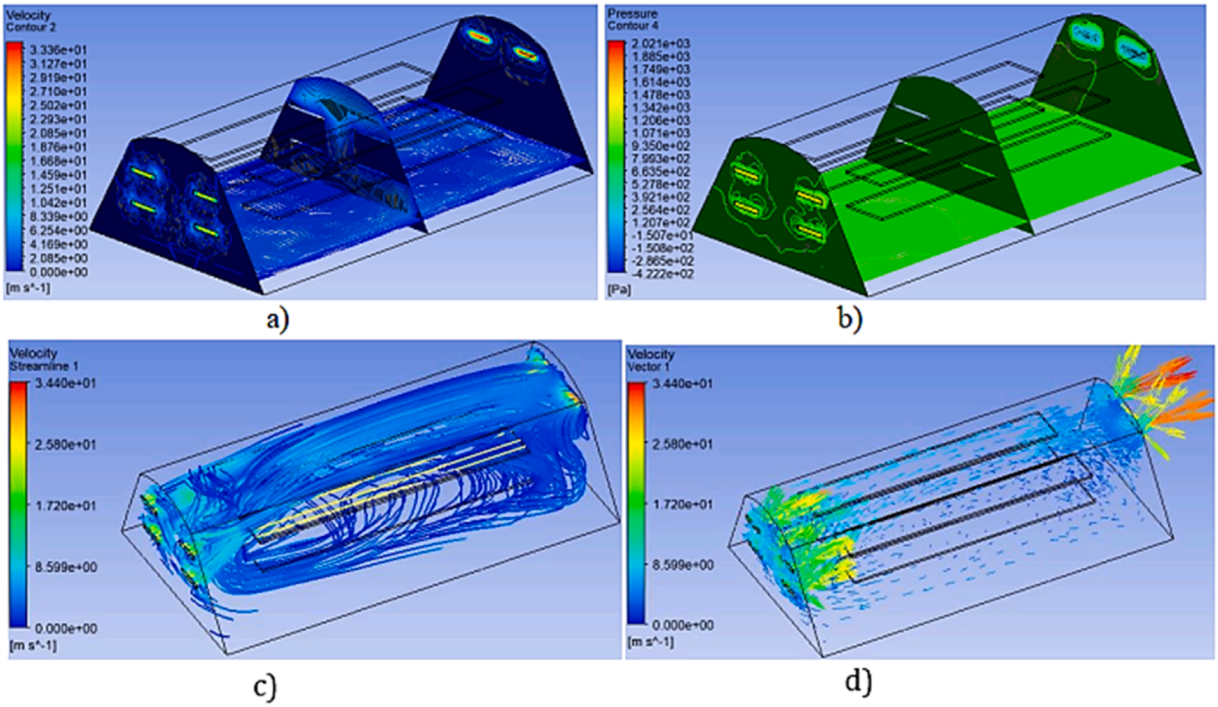

Fig. 21. Contour profile of velocity (a), pressure (b), velocity streamline (c), and vector (d).

each of the four inlet sections. Fig. 21 illustrates the velocity and pressure variations and distribution profiles within the drying chamber and across the outer surface of the briquette walls.

The simulation results indicate that the maximum velocity within the chamber reached 34.4 m/s at the outlet section, while the minimum velocity, recorded near the briquette, cover, and floor wall boundaries, was 0 m/s. The average velocity across the chamber was calculated to be 6.02 m/s. In terms of pressure, the maximum value was observed at the inlet section (2043.4 Pa), while the minimum pressure of −422.24 Pa was recorded at the outlet. The average pressure within the drying chamber of Model 2 was 886 Pa, reflecting a continuous airflow driven by the pressure gradient between the inlet and outlet sections.

Fig. 21 further depicts the velocity streamlines and vectors, showing higher turbulence near the inlet and outlet sections and around the briquettes' front and back surfaces. These regions experience elevated turbulence due to the higher velocities and differences in cross-sectional

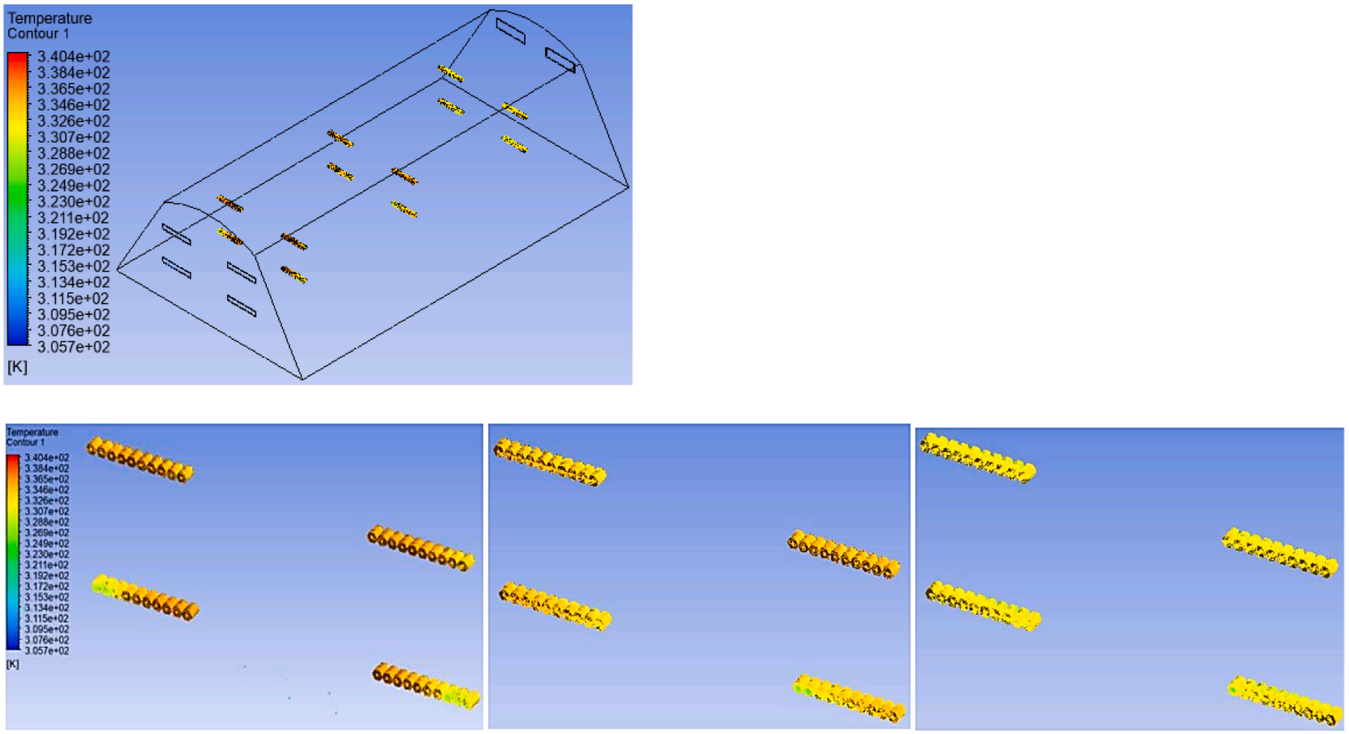

Fig. 22. Temperature contour for Model 3.

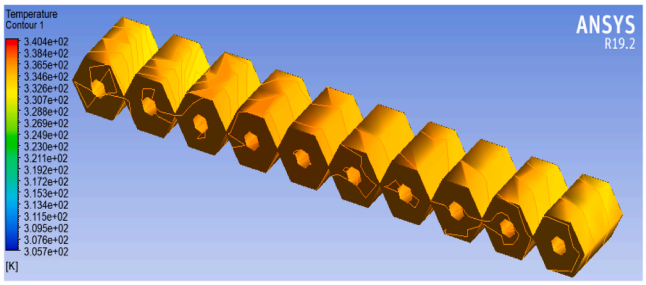

Fig. 23. Temperature contour on the upper front row of briquette.

areas. In contrast, lower turbulence levels were observed across other sections of the chamber and on the briquette surfaces, particularly on the upper bed, where airflow was notably smoother. Compared to Model 1, Model 2 exhibited higher velocity and pressure values at the outlet, although the average velocity was greater in Model 1. This difference can be attributed to the introduction of briquette geometry in Model 2, which disrupts the airflow within the chamber.

3.4. ANSYS simulation results for model 3

3.4.1. Temperature profile

The simulation for Model 3 focused on the drying chamber containing 120 charcoal dust briquette samples provided by Verde Africa Company. The simulation was carried out using the actual shapes of the briquettes and their real arrangement inside the chamber, with conditions reflecting the highest solar radiation levels, specifically on November 14th at noon. The input parameters included a hot air inlet temperature of 68 °C, diffuse radiation of 450 W/m^2, and a constant inlet mass flow rate of 1.35720 kg/s for each of the four inlet sections. Fig. 22 presents the temperature contour of the charcoal briquettes, illustrating both surface and inner temperature variations, including within the cylindrical holes of the briquettes.

The simulation results show that the maximum surface temperature of the briquettes reached 64.2 °C, recorded on the upper front row of the left drying bed. The lowest surface temperature was 43.3 °C, observed on the lower back row of the right drying bed. The average surface temperature across all briquettes was 60.1 °C. Inside the drying chamber, the highest temperature was 65 °C at the inlet section, while the minimum temperature at the outlet was 32.7 °C. The average chamber temperature was 64.2 °C.

Fig. 23 demonstrates a uniform temperature distribution on both the outer surface and inside the cylindrical holes of the briquettes, consistent across all rows. Temperature variations across the chamber, as depicted in Fig. 18, show higher temperatures on the upper front row of the left side (north), driven by the elevated inlet air temperature and the chamber's north-facing orientation. Conversely, the lower back row on the right side (south) exhibited cooler temperatures due to airflow interactions with the briquettes and chamber surfaces, as well as the shading effects within the chamber.

The velocity vector simulation results for the drying chamber with 120 briquettes, depicted in Fig. 24, reveal significant turbulence around the rows of briquettes, particularly near the inlet sections. The airflow pattern, characterized by vectors passing through the cylindrical holes of the hexagonal-shaped briquettes, indicates enhanced convective heat transfer within the inner surfaces of the briquettes. This suggests that the unique airflow pattern contributes to the faster drying of the briquette's interior, optimizing the overall drying efficiency of the system. These findings support the effectiveness of the dryer design in accelerating the drying process by facilitating uniform airflow distribution across and within the drying product.

4. Conclusion

This study employed Computational Fluid Dynamics (CFD) simulations to analyze airflow patterns and temperature distributions within a solar tunnel dryer (STD) designed for drying charcoal briquettes in Mozambique. The results demonstrated that the STD could achieve temperatures ranging from 36.5 °C to 65 °C, with a generally uniform temperature distribution across the briquette surface and within the drying chamber, except near the inlet and outlet sections. Air temperatures inside the chamber remained above 50 °C for up to 7 h per day, enabling a batch of charcoal briquettes to be dried within two days during most months, compared to the traditional 5 to 7 days required for open sun drying. Only June and July, characterized by lower solar radiation, would require extended drying periods.

These findings highlight the potential of the STD to significantly improve production efficiency and energy utilization while reducing drying time. The proposed design could support Mozambique's efforts to promote renewable energy sources, mitigate deforestation, and lower carbon emissions. However, as these results are based on simulation data, experimental validation is recommended to confirm the practical applicability of the design under real-world conditions. While this study focuses on Mozambique, the methodology and findings have broad applicability for other regions with similar climatic conditions and biomass drying needs. By leveraging abundant solar resources, the STD design offers a sustainable, energy-efficient alternative to traditional drying methods, contributing to global efforts in renewable energy adoption and environmental conservation.

Future work

In the future, the system will be designed, constructed, and experimentally tested for drying briquettes. Research will focus on upscaling the solar tunnel dryer, conducting field testing, and optimizing its performance under various operational conditions. These studies will be crucial for validating the simulation results and ensuring the system performs efficiently in real-world applications. Furthermore, such work will aid in refining the design for broader deployment and assessing its viability for large-scale production of charcoal briquettes.

CRediT authorship contribution statement

Jimmy Chaciga: Writing – review & editing, Validation, Formal

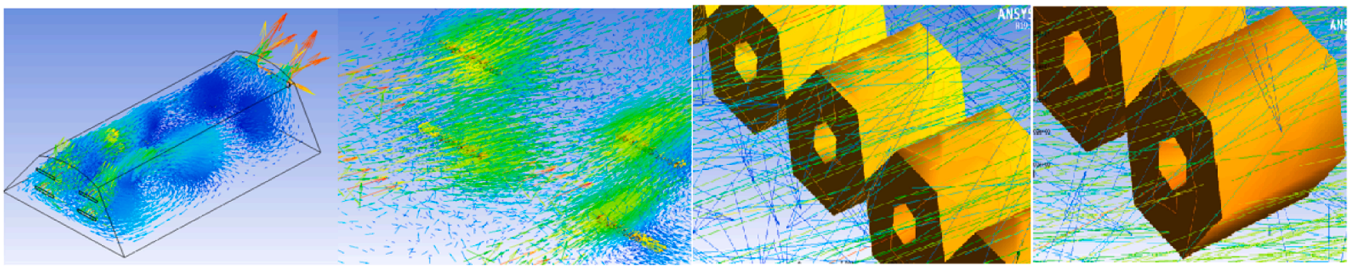

Fig. 24. Velocity Vector for Model 3.

analysis, Data curation, Conceptualization. **G. Jeffrey Snyder:** Writing – review & editing, Validation, Supervision, Software, Resources, Formal analysis, Conceptualization. **Francis Wanjala Nyongesa:** Writing – review & editing, Supervision, Project administration, Conceptualization. **Sebastian Waita:** Writing – review & editing, Validation, Supervision, Resources, Conceptualization. **Fauzia Argentina Guibunda:** Writing – review & editing, Writing – original draft, Visualization, Validation, Methodology, Investigation, Formal analysis, Data curation, Conceptualization.

Declaration of Competing Interest

The authors declare that they have no known competing financial interests or personal relationships that could have appeared to influence the work reported in this paper.

Acknowledgment

The authors gratefully acknowledge the financial support provided by the Regional Scholarship and Innovation Fund (RSIF) and extend their appreciation to the University of Nairobi, Kenya for its academic supervision. Special thanks to Northwestern University, USA for their laboratory and facilities, which made the computational simulations possible.

Data availability

Data will be made available on request.

References

Ameri, B., Hanini, S., Benhamou, A., Chibane, D., 2018. Comparative approach to the performance of direct and indirect solar drying of sludge from sewage plants, experimental and theoretical evaluation. Sol. Energy 159 (ember 2017), 722–732. https://doi.org/10.1016/j.solener.2017.11.032.

Aukah, J., Muvengei, M., Ndiritu, H., Onyango, C., 2018. Prediction of Airflow and Temperature Distribution in Solar Biomass Hybrid Dryer using Computational Fluid Dynamics. J. Sustain. Res. Eng. 4 (3), 76–89.

Bala, B.K., Debnath, N., 2012. Solar Drying Technology: Potentials and Developments. J. Fundam. Renew. Energy Appl. 2, 1–5. https://doi.org/10.4303/jfrea/r120302.

Balocco, C., Mercatelli, L., Azzali, N., Meucci, M., Grazzini, G., 2018. Experimental transmittance of polyethylene films in the solar and infrared wavelengths. Sol. Energy 165 (March)), 199–205. https://doi.org/10.1016/j.solener.2018.03.011.

Dhar, A., Naeth, M.A., Jennings, P.D., Gamal El-Din, M., 2020. Perspectives on environmental impacts and a land reclamation strategy for solar and wind energy systems. Sci. Total Environ. 718, 134602. https://doi.org/10.1016/j.scitotenv.2019.134602.

Duong, Y.H.P., Vo, N.T., Le, P.T.K., Tran, V.T., 2021. Three-dimensional simulation of solar greenhouse dryer. Chem. Eng. Trans. 83, 211–216. https://doi.org/10.3303/CET2183036.

Ekechukwu, O.V., 1999. Review of solar-energy drying systems I: An overview of drying principles and theory. Energy Convers. Manag. 40 (6), 593–613. https://doi.org/10.1016/S0196-8904(98)00092-2.

Gunnarsson, A., Andersson, K., Adams, B.R., Fredriksson, C., 2020. Discrete-ordinates modelling of the radiative heat transfer in a pilot-scale rotary kiln. Energies 13 (9), 1–18. https://doi.org/10.3390/en13092192.

Janjai, S., Lamlert, N., Intawee, P., Mahayothee, B., Bala, B.K., Nagle, M., Müller, J., 2009. Experimental and simulated performance of a PV-ventilated solar greenhouse dryer for drying of peeled longan and banana. Sol. Energy 83 (9), 1550–1565. https://doi.org/10.1016/j.solener.2009.05.003.

Kasaeian, A., Sharifi, S., Yan, W.M., 2018. Novel achievements in the development of solar ponds: A review. Sol. Energy 174 (August), 189–206. https://doi.org/10.1016/j.solener.2018.09.010.

Lamrani, B., Elmrabet, Y., Mathew, I., Bekkioui, N., Etim, P., Chahboun, A., Draoui, A., Ndukwu, M.C., 2022. Energy, economic analysis and mathematical modelling of mixed-mode solar drying of potato slices with thermal storage loaded V-groove collector: Application to Maghreb region. Renew. Energy 200 (August), 48–58. https://doi.org/10.1016/j.renene.2022.09.119.

Mehdipour, R., Ghaffari, A., 2021. Solar dryer performance simulation: Experimental and numerical study. J. Food Process Eng. 44 (11), 1–18. https://doi.org/10.1111/jfpe.13875.

Mewa, E.A., Okoth, M.W., Kunyanga, C.N., Rugiri, M.N., 2019. Experimental evaluation of beef drying kinetics in a solar tunnel dryer. Renew. Energy 139, 235–241. https://doi.org/10.1016/j.renene.2019.02.067.

Mohana, Y., Mohanapriya, R., Anukiruthika, T., Yoha, K.S., Moses, J.A., Anandharamakrishnan, C., 2020. Solar dryers for food applications: Concepts, designs, and recent advances. Sol. Energy 208 (February), 321–344. https://doi.org/10.1016/j.solener.2020.07.098.

Monish, M., Ramnath, S., Manojkumar, S.V., Jeeva, B., 2018a. Solar tunnel air dryer: A computational fluid dynamics investigation for the flow path design with the temperature distribution. Int. J. Mech. Prod. Eng. Res. Dev. 8 (7), 263–273 (Special Issue).

Monish, M., Ramnath, S., Manojkumar, S.V., Jeeva, B., 2018b. Solar tunnel air dryer: A computational fluid dynamics investigation for the flow path design with the temperature distribution. Int. J. Mech. Prod. Eng. Res. Dev. 8 (7), 263–273 (Special Issue).

Ndukwu, M.C., Diemuodeke, E.O., Abam, F.I., Abada, U.C., Eke-emezie, N., Simo-Tagne, M., 2020. Development and modelling of heat and mass transfer analysis of a low-cost solar dryer integrated with biomass heater: Application for West African Region. Sci. Afr. 10, e00615. https://doi.org/10.1016/j.sciaf.2020.e00615.

Ortiz-Rodríguez, N.M., Condorí, M., Durán, G., García-Valladares, O., 2022. Solar drying Technologies: A review and future research directions with a focus on agroindustrial applications in medium and large scale. Appl. Therm. Eng. 215 (March). https://doi.org/10.1016/j.applthermaleng.2022.118993.

Patel, A., Patel, G., 2014. Operational Augmentation of Forced Circulation Type Solar Dryer System Using CFD Analysis. *J. Eng. Res. Appl.* 4 (4), 265–268 (Www.Ijera.Com). ⟨www.ijera.com⟩.

Raj, A.K., Srinivas, M., Jayaraj, S., 2019. CFD modeling of macro-encapsulated latent heat storage system used for solar heating applications. Int. J. Therm. Sci. 139 (October 2018), 88–104. https://doi.org/10.1016/j.ijthermalsci.2019.02.010.

Rathore, N.S., Panwar, N.L., 2010. Experimental studies on hemi cylindrical walk-in type solar tunnel dryer for grape drying. Appl. Energy 87 (8), 2764–2767. https://doi.org/10.1016/j.apenergy.2010.03.014.

Tran, V.T., Duong, Y.H.P., Le, T.M., 2021. The Influence of Meshing Strategies on the Numerical Simulation of Solar Greenhouse Dryer. IOP Conf. Ser.: Earth Environ. Sci. 947 (1). https://doi.org/10.1088/1755-1315/947/1/012007.

Tuncer, A.D., Sözen, A., Afshari, F., Khanlari, A., Şirin, C., Gungor, A., 2020. Testing of a novel convex-type solar absorber drying chamber in dehumidification process of municipal sewage sludge. J. Clean. Prod. 272. https://doi.org/10.1016/j.jclepro.2020.122862.

Zziwa, A., Okello, A.W., Kabenge, I., Matsapwe, D., Kizito, S.S., Paul, S., Kambugu, R.K., 2023. Optimizing Solar Drying: A Critical Review of Shapes, Orientation, and Future Prospects for Hybrid Solar Dryers. J. Power Energy Eng. 11 (12), 44–63. https://doi.org/10.4236/jpee.2023.1112004.